Pressure-induced superconductivity in the metal thiophosphate $Pb_2P_2S_6$

Xinyi He,[1] Zhitao Zhang [ORCID],[2] Zhenyu Ding,[2] Shuyang Wang,[2] Chunhua Chen,[2] Xuliang Chen [ORCID],[2] Yonghui Zhou,[2] Chao An,[1] Min Zhang [ORCID],[1] Ying Zhou [ORCID],[1,*] Xiaoping Yang,[2] and Zhaorong Yang[1,2,3,†]

[1]*Institutes of Physical Science and Information Technology, Anhui University, Hefei 230601, China*
[2]*Anhui Province Key Laboratory of Condensed Matter Physics at Extreme Conditions, High Magnetic Field Laboratory, HFIPS, Chinese Academy of Sciences, Hefei 230031, China*
[3]*Collaborative Innovation Center of Advanced Microstructures, Nanjing 210093, China*

We report on the pressure-tuning of the physical properties of a metal thiophosphate $Pb_2P_2S_6$. Resistance measurements evidence a semiconducting-to-metallic transition at around 39 GPa and immediate emergence of superconductivity. The superconducting critical temperature T_C monotonously increases from 3.2 to 5.1 K until the highest studied pressure 54 GPa. Over the whole pressure range, the pristine monoclinic lattice symmetry is not changed. Moreover, the resonance Raman scattering is observed in the range of 8–12 GPa depending on the excitation energy used. These findings establish $Pb_2P_2S_6$ as a new platform to explore intrinsic metallization and superconductivity, which may promote developments of relevant applications.

I. INTRODUCTION

The metal phosphates $M_2P_2X_6$ (M represents a metal, and $X =$ S, Se) have stimulated both fundamental and applied interest [1–9]. These compounds are chemically robust semiconductors with a wide band gap in excess of 1.0 eV [4,10,11]. Depending on the cation M, the crystal structures of these materials can be categorized into two classes, namely the layered two-dimensional (2D) monoclinic structure where M denotes 3d transition metals such as Fe, Ni, or Mn [12,13] and the 3D monoclinic structure where M denotes Sn or Pb [11,14]. Among them, the 2D members exhibit rich magnetic properties which are benefit for applications in spintronic and magnetic devices [15–20]. Besides, the layered structure also allows to accommodate extrinsic intercalated species with potential applications as field effect transistors, UV photodetectors, and photocatalysts for water splitting [9,21–23]. Whereas the 3D members possess advanced optical characteristics and pronounced ferroelectric properties, and thus offer wide application prospects in optoelectronics, photocatalysis as well as tunable capacitances [6,7,11,24–27].

Fundamentally, rich physics including Mott insulator-to-metal transition, spin crossover, and complex structural transition can occur in these compounds when the hosting lattice is tuned by applied pressure [13,28–36]. In $FePSe_3$, for example, when a 2D to 3D structural transition is driven by an applied pressure of $\sim$9.0 GPa, the magnetic moments vanish and simultaneously superconductivity develops [13,35]. For $Pb_2P_2S_6$ which has a 3D phosphate structure, high-pressure Raman experiments revealed unusual enhancements of spectral intensity below 20 GPa for unknow reasons and discontinuous frequency jumps above 20 GPa likely due to changes of the crystal structure [37]. Density functional theory

calculations predicted a metallization of the system at 65 GPa, but no transport measruements were preformed at such high pressures and at cryogenic temperatures [37].

In this paper, we grew high-quality single crystalline sample of $Pb_2P_2S_6$ and performed comprehensive high-pressure electrical resistance, x-ray diffraction (XRD), and Raman measurements to investigate the pressure evolution of electronic and structural properties. We find no signature of structural transition below $\sim$55 GPa by XRD and Raman measurements. Upon compression, $Pb_2P_2S_6$ undergoes a semiconducting-to-metallic transition at $\sim$39 GPa and immediately superconductivity with critical temperature T_C of 3.2 K is observed. Further compression results in a monotonous increase of T_C to 5.1 K at 54.0 GPa. Resonance Raman intensity enhancements are also observed and discussed.

II. EXPERIMENTAL AND CALCULATION METHODS

Single crystals of $Pb_2P_2S_6$ were synthesized via the chemical vapor transport technique with iodine as a transport agent [8]. A stoichiometric amount of high-purity elemental powders (mole ratio Pb: P: S = 1: 1: 3, around 1 g in total) and iodine (about 10 mg) were sealed into a vacuum quartz tube. The tube was placed in a two-zone furnace with a temperature gradient from 700 °C to 600 °C for 6 days. Single crystals with millimeter size have been collected at the cold end of the quartz tube, as shown in the inset of Fig. 1(a). The XRD of the samples at ambient pressure was measured in a Rigaku x-ray diffractometer with Cu $K\alpha$ radiation of wavelength $\lambda = 1.5406$ Å. The atomic proportion of the crystals crystal was characterized by energy dispersive x-ray spectroscopy (EDXS) with the area and point scanning modes.

High-pressure electrical transport experiments were carried out in a nonmagnetic Be-Cu diamond-anvil cell with a pair of anvil culets of 300 μm. The four-probe method was applied on a piece of single crystal with dimensions of

---

*Corresponding author: yzhou@ahu.edu.cn
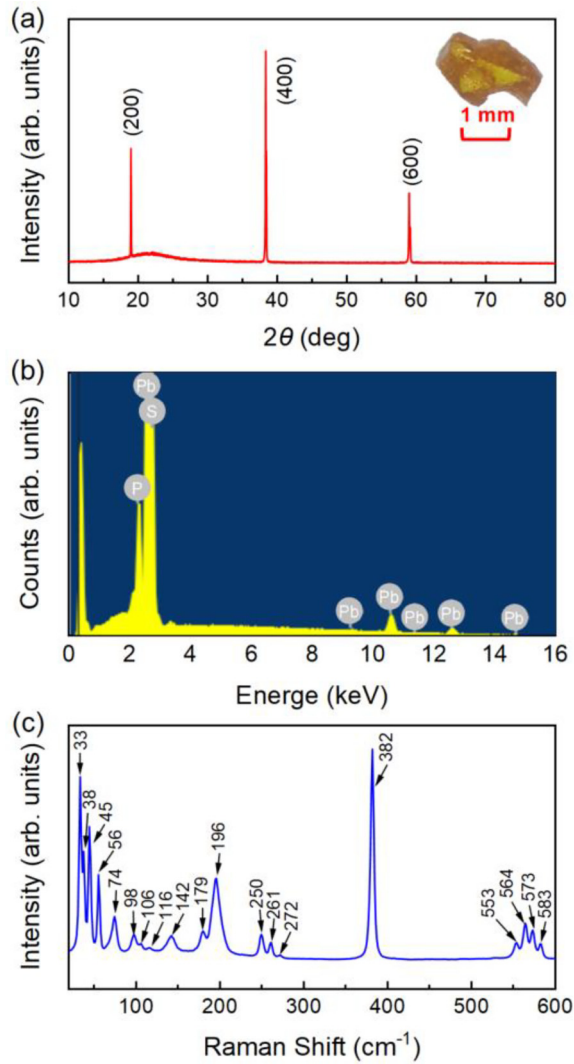†Corresponding author: zryang@issp.ac.cn

FIG. 1. (a) XRD pattern for a $Pb_2P_2S_6$ single crystal. Inset: an optic image of the single crystal. (b) Energy-dispersive x-ray spectroscopy and (c) Raman spectrum for the $Pb_2P_2S_6$ single crystal.

FIG. 2. (a) Temperature-dependent resistance curves $R(T)$ for a $Pb_2P_2S_6$ single crystal in the pressure range of (a) 23.3–33.3 GPa, and (b) 39.4–54.0 GPa. The inset of (b) displays the zoomed-in view of the $R(T)$ curves in the low-temperature range.

$80 \times 70 \times 10 \, \mu m^3$ to collect the low-temperature resistance measurements in an in-house 9-T transport property measurement system. High-pressure angle-dispersive synchrotron XRD and Raman scattering measurements were performed in symmetric diamond anvil cells with Daphne 7373 as the transmitting medium. Synchrotron XRD experiments were conducted with powdered crystals at beamline BL15U1 of the Shanghai Synchrotron Radiation Facility ($\lambda = 0.6199$ Å). The DIOPTAS [38] program was employed for image integrations and the XRD patterns were fitted by using the RIETICA program with the LeBail method [39]. The Raman spectra were recorded with cleaved single-crystal flakes by using a commercial Renishaw Raman spectrometer (laser excitation wavelength $\lambda = 532$ and 633 nm). Pressure was applied at room temperature and calibrated by using the Ruby luminescence method in all high-pressure experiments [40].

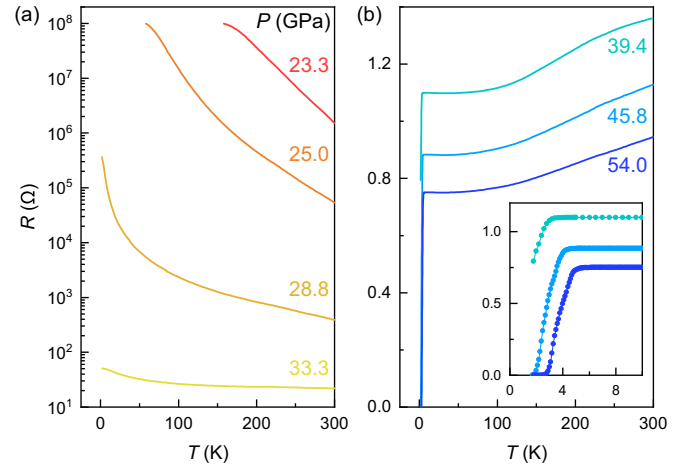Single point energy and Hellmann-Feynman force under pressure were calculated by using the Vienna *ab initio* Simulation Package (VASP) [41,42] within the framework of generalized gradient approximation (Perdew-Burke-Ernzerhof exchange functional) [43]. The ion-electron interaction was modeled by the projector augmented wave method [44,45] with a uniform energy cutoff of 340 eV. Spacing between k points was $0.015 \, Å^{-1}$. The geometry structures were optimized by employing the conjugate gradient technique, and in the final geometry, no force on the atoms exceeded 0.001 eV/Å. The phonon vibrational spectrum is investigated by using the finite displacement method implemented in the PHONOPY package [46].

III. RESULTS AND DISCUSSION

The as-grown $Pb_2P_2S_6$ single crystals were characterized by XRD, EDXS, and Raman spectrum. As shown in the inset of Fig. 1(a), the $Pb_2P_2S_6$ single crystal is transparent yellow, which reflects the large band gap of ~ 2.6 eV [8,11]. The single-crystal XRD pattern displayed in Fig. 1(a) contains only ($l00$) peaks, indicating that the bc plane is a natural cleavage facet. The EDXS in Fig. 1(b) yields an actual chemical composition of $Pb_{1.9}P_2S_{6.3}$ for the single crystals, which is very close to the stoichiometry. The Raman spectrum collected on the $Pb_2P_2S_6$ single crystal given in Fig. 1(c) shows 19 observable Raman modes in the range of 20–800 cm^{-1}. All of the Raman modes are consistent with those in previous reports [37,47]. These results indicate the high quality of the single crystals.

We performed high-pressure resistance measurements on a $Pb_2P_2S_6$ single crystal to investigate the pressure evolution of the electronic properties. Figure 2 depicts the temperature-dependent resistance curves $R(T)$ of the sample at different pressures. At initial pressures, the extremely large resistance arising from the wide band gap of ~ 2.6 eV exceeds the measuring range of our instrument ($< 10^8 \, \Omega$) [8,11]. When pressure is increased to 23.3 GPa, the room temperature resistance becomes measurable as $\sim 10^6 \, \Omega$. Upon cooling the resistance increases, characterizing a semiconducting behavior. As pressure is raised, the magnitude of the whole
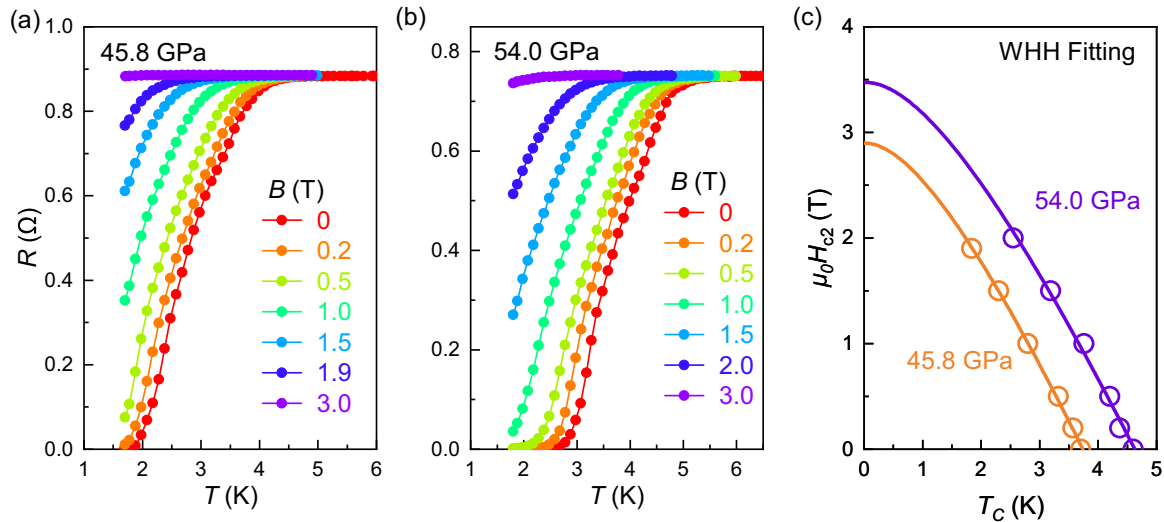
FIG. 3. Magnetic field evolution of the resistive superconducting transition measured at selected pressures of (a) 45.8 GPa, and (b) 54.0 GPa. (c) Temperature-dependent upper critical field $\mu_0 H_{c2}(T)$ extracted from the data in (a) and (b). For determination of the superconducting critical temperature, $T_c^{90\%}$ where resistance drops to 90% of the normal-state resistance are used. The solid lines correspond to the fitting to the Werthamer-Helfand-Hohenberg (WHH) model [48].

$R(T)$ curve is dramatically suppressed. When pressure reaches 39.4 GPa, the semiconducting behavior is replaced by a metallic behavior, namely the resistance decreases upon cooling. Interestingly, the occurrence of metallization is accompanied by a resistance drop below ∼3.2 K, as is shown in the inset of Fig. 2(b). For a higher pressure of 45.8 GPa, the resistance vanishes completely below 1.9 K which characterizes presence of superconductivity. As pressure is further raised, both the onset temperature of the superconducting transition, T_c^{onset}, and the zero-resistance temperature T_c^{zero} display monotonous increments until the highest studied pressure of 54.0 GPa.

Figures 3(a) and 3(b) present the magnetic field evolution of the low-temperature $R(T)$ curves for selected pressures of 45.8 GPa, and 54.0 GPa. It can be seen that as the magnetic field increases the zero-resistance state is gradually suppressed, which further proves that the zero-resistance state arises from superconductivity. The upper critical field $\mu_0 H_{c2}$ as a function of critical temperature $T_c^{90\%}$ is shown in Fig. 3(c). By fitting the data to the Werthamer-Helfand-Hohenberg (WHH) model [48], the zerotemperature limit of upper critical magnetic field $\mu_0 H_{c2}(0)$ are estimated to be 2.9 T and 3.5 T, respectively for 45.8 GPa and 54.0 GPa. Both values are much lower than the corresponding Pauli limit field $\mu_0 H_{c2}(0) = 1.84 T_c$, indicating the absence of Pauli pair breaking [49].

In order to uncover the underlying structural evolution, we carried out high-pressure synchrotron XRD and Raman scattering measurements at pressures up to 55.9 GPa. Figure 4(a) presents the representative XRD patterns measured at different pressures on powdered $Pb_2P_2S_6$ crystals. At initial pressure 0.8 GPa, the XRD pattern can be well indexed by the monoclinic structure with space group $P2_1/c$ (No. 14), which is exactly the same as that at ambient pressure. With increasing pressure, all the diffraction peaks shift to a higher angle, which corresponds to a continuous shrinkage of the lattice under pressure. Over the whole pressure range,

no new Bragg peaks appear and all the XRD patterns can be well fitted with the $P2_1/c$ phase. Typical analysis of the XRD patterns at 0.8, 15.7, 30.8, and 49.6 GPa are shown in Supplemental Material Fig. S1 [50]. These results prove that no structural transition occurs below 55.9 GPa in $Pb_2P_2S_6$. The pressure dependences of lattice parameters a, b, c, and unit-cell volume V determined by fittings are presented in Figs. 4(b) and 4(c). All these parameters decline continuously with increasing pressure. The unit-cell volume V as a function of pressure can be fitted by the third-order Birch-Murnaghan
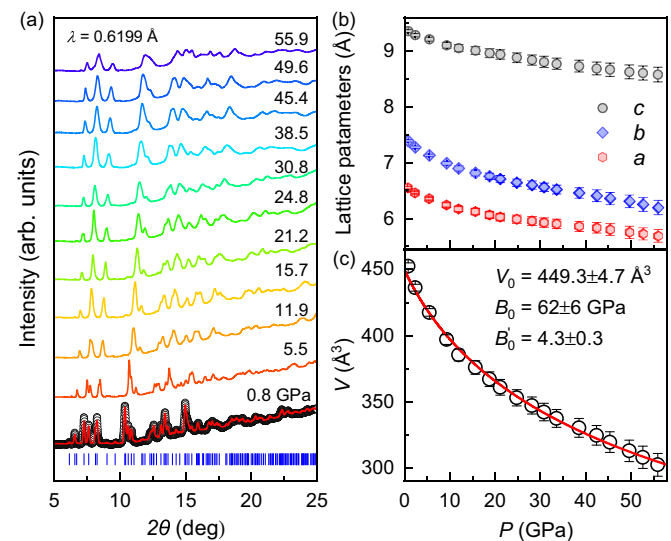

FIG. 4. (a) Synchrotron x-ray diffraction (XRD) patterns under pressures up to 55.9 GPa, which were measured on powdered $Pb_2P_2S_6$ crystals at room temperature. For 0.8 GPa, the red line presents the fitting to the data and the blue vertical bars indicate the diffraction peak positions. (b) Pressure dependences of lattice parameters a, b, and c. (c) Pressure dependence of the lattice volume V. The solid red line represents the fitting curve based on the third-order Birch-Murnaghan equation of state.
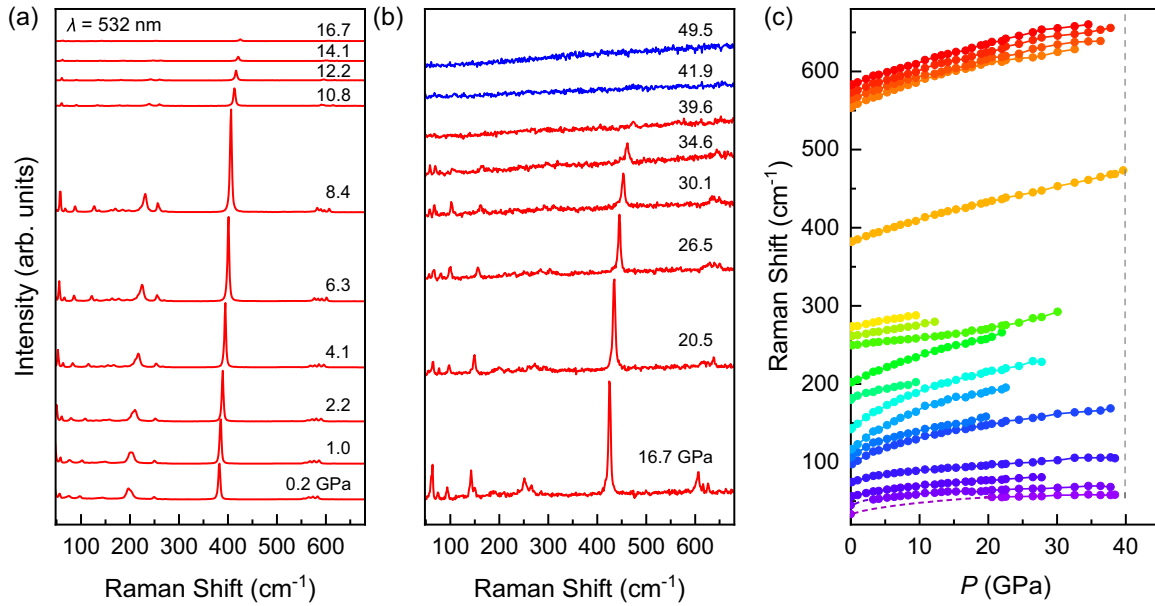
FIG. 5. Raman spectra (Run 1) measured on the $Pb_2P_2S_6$ single crystal (a) from 0.2 to 16.7 GPa and (b) from 16.7 to 49.5 GPa. The measurements were performed with a laser wavelength of $\lambda = 532$ nm (or laser energy 2.33 eV) at room temperature. (c) Pressure-dependent Raman shifts for all the detected modes.

equation of state [51], as indicated by the solid red line in Fig. 4(c). The fitting yields the ambient pressure volume $V_0 = 449.3 \pm 4.7$ Å^3, bulk modulus $B_0 = 62 \pm 6$ GPa, and the first-order derivative of the bulk modulus at zero pressure $B_0' = 4.3 \pm 0.3$. Moreover, we performed theoretical calculations on the phonon spectrum of pressurized $Pb_2P_2S_6$ at 0 and 55 GPa. As shown in Supplemental Material Fig. S2 [50], the calculated phonon spectra are stable without imaginary frequency, indicating that $Pb_2P_2S_6$ is dynamically stable in the monoclinic structure up to 50 GPa. These results indicate no structure phase transition under pressure, thus ruling out the structural origin of the pressure-induced superconductivity in $Pb_2P_2S_6$.

Figures 5(a) and 5(b) present the high-pressure Raman spectra of the $Pb_2P_2S_6$ single crystal measured with excitation wavelength of 532 nm (Run 1). At 0.2 GPa, the Raman spectrum is consistent with that measured at ambient condition, as is shown in Fig. 1(c). By using Lorenz fitting to the data, the Raman shifts are extracted and plotted as functions of pressure in Fig. 5(c).With increasing pressure, all the modes continuously shift towards higher wavenumber, indicative of strengthening of the corresponding bonds. In agreement with the XRD results, no new Raman mode is detected below 39.6 GPa, providing additional evidence for the absence of structural transition in $Pb_2P_2S_6$. For higher pressures, the Raman signals rapidly disappear. Since no structural transition is involved, the loss of Raman signals could be ascribed to the metallization of the sample [37,52]. In fact, as is revealed by the transport measurements, the metallization of the sample takes place at almost the same pressure of 39.4 GPa. In addition, in order to confirm the observation of continuous evolution of Raman modes with pressure, we have further carried out an independent run of high-pressure Raman scattering measurement, which is referred to as "Run 2". Figures S3(a) and S3(b) display the Raman spectra at pressures ranging from

0.5 to 45.5 GPa for Run 2. In this run, the disappearance of Raman signals and the continuous evolution of Raman modes were reproducible.

It is noticed that the Raman spectral intensity for most of the detected modes exhibit an unusual enhancement with increasing pressure below 8.4 GPa, whereas further compression causes suppression effects. To show this feature more clearly, the pressure dependence of the Raman spectral intensity for a typical mode (e.g. the strongest mode at $382\,cm^{-1}$) is illustrated in Fig. S5(b). Generally, an enhancement of Raman spectral intensity may have different origins such as (i) structural phase transitions, (ii) depolarization effect, and/or (iii) resonance Raman scattering effect [53–56]. According to the XRD and Raman evidences shown above, the possibility of a structural transition as an origin can be firstly ruled out. Secondly, if depolarization effect is the orgin, then the depolarization ratio between the perpendicular and parallel components of the Raman intensity should also exhibit a significant pressure dependence. However, as is displayed in Fig. S4(c) [50], the depolarization ratio for the typical mode $382\,cm^{-1}$ is almost constant over pressure, which is in sharp contrast with the case where a Raman enhancement is caused by depolarization effect [56]. Thirdly, in case the unusual Raman enhancements observed in present work are due to resonance Raman scattering, there should exist an underlying electronic absorption band which has a transition energy close to that of the Raman excitation 532 nm (or 2.33 eV) [53,56,57]. For comparison, high-pressure Raman spectra with a different excitation wavelength of 633 nm (or ~1.96 eV) are measured and displayed in Fig. S5 [50]. As is expected, the maximum of the Raman enhancements appears at a higher pressure of 12.2 GPa, which indicates that the transition energy of the resonance absorption band is gradually reduced upon compression. Further analysis of resonance Raman in the Supplemental Material [50] shows
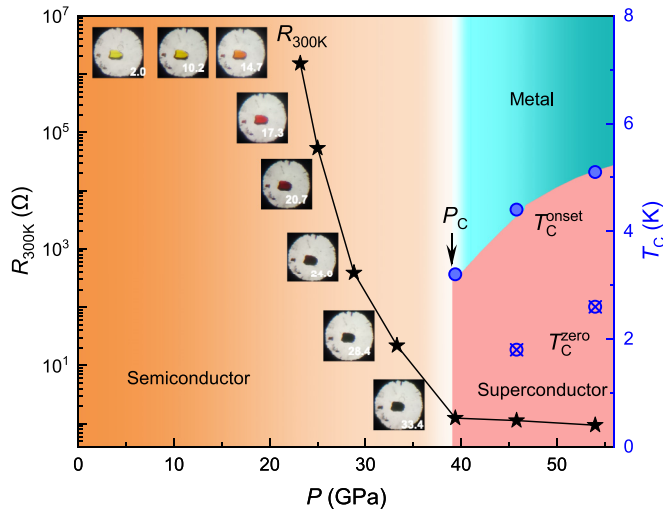
FIG. 6. The pressure evolution phase diagram for $Pb_2P_2S_6$. The left axis represents the values of resistance at 300 K. The right axis corresponds to the onset superconducting critical temperature T_c^{onset} and zero-resistance temperature T_c^{zero}. The insets display optical micrographs of the $Pb_2P_2S_6$ sample at different pressures.

that this resonance absorption transition may be associated with the band gap of this sample.

Based on the data presented here, we construct a pressure evolution phase diagram for $Pb_2P_2S_6$, as displayed in Fig. 6. Optical micrographs of the $Pb_2P_2S_6$ single crystal are also included to indicate the color change of the sample at different pressures. As mentioned above, the crystal at ambient pressure is partially transparent with a yellow color [see the inset of Fig. 1(a)]. Upon compression, the color of the sample gradually varies from light-yellow to orange (at 14.7 GPa) then to dark-red (at 20.7 GPa). For higher pressures, the crystal becomes darker and darker before being opaque black above 28.4 GPa. Such a piezochromic transition implies a gradual closure of the band gap. In accordance with the piezochromic phenomenon, the resistance at 300 K ($R_{300 K}$) rapidly decreases with pressure, namely from 1.5 MΩ (at 23.2 GPa) to 1.2 Ω (at 39.4 GPa). Afterwards, metallization and superconductivity are simultaneously observed. Superconductivity is monotonously enhanced by increasing pressure. Eventually, T_c^{onset} reaches a maximum of 5.1 K. It should be noted that all of these evolutions occur in the same lattice symmetry, namely the monoclinic $P2_1/c$ phase of $Pb_2P_2S_6$.

IV. CONCLUSION

In summary, we have synthesized $Pb_2P_2S_6$ single crystals and investigated the high-pressure electrical transport and structural properties. We find that application of pressure induces metallization and superconductivity at around 39 GPa. The superconducting T_C is monotonously enhanced from 3.2 to 5.1 K throughout the pressure range of 39–54 GPa. X-ray diffraction and Raman results consistently prove the absence of structural transition over the studied pressure. Observations of unusual enhancements of Raman intensity are correlated with resonance Raman effect. These findings establish $Pb_2P_2S_6$ as a special member of the metal phosphates. Firstly, superconductivity emerges from the pristine 3D metal phosphate structure without structural transition. Secondly, the resonance Raman effect provides an additional avenue to gain information of the underlying electronic structure. Thirdly, the rich and interrelated physics, including piezochromism, resonance Raman scattering, metallization, and superconductivity, make $Pb_2P_2S_6$ a highly tunable electronic material which may promote applications such as in optoelectronics.

[1] S. M. Kang, K. W. Kim, B. H. Kim, J. Kim, K. I. Sim, J.-U. Lee, S. Lee, K. Park, S. Yun, T. Kim, A. Nag, A. Walters, M. Garcia-Fernandez, J. Li, L. Chapon, K.-J. Zhou, Y.-W. Son, J. H. Kim, H. Cheong, and J.-G. Park, Nature (London) **583**, 785 (2020).

[2] T. T. Mai, K. F. Garrity, A. McCreary, J. Argo, J. R. Simpson, V. Doan-Nguyen, R. V. Aguilar, and A. R. H. Walker, Sci. Adv. **7**, eabj3106 (2021).

[3] X. Z. Wang, J. Cao, H. Li, Z. G. Lu, A. Cohen, A. Haldar, H. Kitadai, Q. Tan, K. S. Burch, D. Smirnov, W. G. Xu, S. Sharifzadeh, L. B. Liang, and X. Ling, Sci. Adv. **8**, eabl7707 (2022).

[4] M. A. Susner, M. Chyasnavichyus, M. A. McGuire, P. Ganesh, and P. Maksymovych, Adv. Mater. **29**, 1602852 (2017).

[5] K. Kim, S. Y. Lim, J.-U. Lee, S. Lee, T. Y. Kim, K. Park, G. S. Jeon, C.-H. Park, J.-G. Park, and H. Cheong, Nat. Comm. **10**, 345 (2019).

[6] K. Z. Rushchanskii, Y. M. Vysochanskii, and D. Strauch, Phys. Rev. Lett. **99**, 207601 (2007).

[7] P. L. Wang, Z. F. Liu, P. Chen, J. A. Peters, G. J. Tan, J. Im, W. W. Lin, A. J. Freeman, B. W. Wessels, and M. G. Kanatzidis, Adv. Funct. Mater. **25**, 4874 (2015).

[8] B. Ji, A. Sarkar, K. Wu, A. Swindle, and J. Wang, Dalton Trans. **51**, 4522 (2022).

[9] X. Zhang, X. D. Zhao, D. H. Wu, Y. Jing, and Z. Zhou, Adv. Sci. **3**, 1600062 (2016).

[10] K.-z. Du, X.-z. Wang, Y. Liu, P. Hu, M. I. B. Utama, C. K. Gan, Q. H. Xiong, and C. Kloc, ACS Nano **10**, 1738 (2016).

[11] P. Wang, M. Abudoureheman, and Z. H. Chen, Dalton Trans. **49**, 17221 (2020).

[12] G. Ouvrard, R. Brec, and J. Rouxel, Mat. Res. Bull. **20**, 1181 (1985).

[13] Y. S. Zheng, X.-x. Jiang, X.-x. Xue, J. Y. Dai, and Y. X. Feng, Phys. Rev. B **100**, 174102 (2019).

[14] C. D. Carpentier and R. Nitsche, Mater. Res. Bull. **9**, 401 (1974).

[15] S. Calder, A. V. Haglund, A. I. Kolesnikov, and D. Mandrus, Phys. Rev. B **103**, 024414 (2021).

[16] X. Z. Wang, K. Z. Du, Y. Y. Fredrik Liu, P. Hu, J. Zhang Q. Zhang, M. H. S. Owen, X. Lu, C. K. Gan, P. Sengupta, C. Kloc, and Q. H. Xiong, 2D Mater. **3**, 031009 (2016).

[17] D. Lançon, H. C. Walker, E. Ressouche, B. Ouladdiaf, K. C. Rule, G. J. McIntyre, T. J. Hicks, H. M. Rønnow, and A. R. Wildes, Phys. Rev. B **94**, 214407 (2016).

[18] A. R. Wildes, V. Simonet, E. Ressouche, G. J. Mcintyre, M. Avdeev, E. Suard, S. A. J. Kimber, D. Lancon, G. Pepe, B. Moubaraki, and T. J. Hicks, Phys. Rev. B **92**, 224408 (2015).

[19] A. R. Wildes, H. M. Rønnow, B. Roessli, M. J. Harris, and K. W. Godfrey, Phys. Rev. B **74**, 094422 (2006).

[20] X. X. Li, X. J. Wu, and J. L. Yang, J. Am. Chem. Soc. **136**, 11065 (2014).

[21] R. Kumar, R. N. Jenjeti, M. P. Austeria, and S. Sampath, J. Mater. Chem. C **7**, 324 (2019).

[22] M. Barua, M. M. Ayyub, P. Vishnoi, K. Pramoda, and C. N. R. Rao, J. Mater. Chem. A **7**, 22500 (2019).

[23] J. Liu, X.-B. Li, D. Wang, W.-M. Lau, P. Peng, and L.-M. Liu, J. Chem. Phys. **140**, 054707 (2014).

[24] Y. D. Xu, X. Fu, H. J. Zheng, Y. H. He, W. W. Lin, K. M. McCall, Z. F. Liu, S. Das, B. W. Wessels, and M. G. Kanatzidis, ACS Photonics **5**, 566 (2017).

[25] P. L. Wang, S. S. Kostina, F. Meng, O. Y. Kontsevoi, Z. F. Liu, P. Chen, J. A. Peters, M. Hanson, Y. H. He, D. Y. Chung, A. J. Freeman, B. W. Wessels, and M. G. Kanatzidis, Cryst. Growth Des. **16**, 5100 (2016).

[26] I. Martynyuk-Lototska, O. Mys, B. Zapeka, M. Kostyrko, A. Grabar, and R. Vlokh, Appl. Opt. **53**, B103 (2014).

[27] M. G. Sendeku, F. Wang, Z. Cheng, P. Yu, N. Gao, X. Zhan, Z. Wang, and J. He, ACS Appl. Mater. Interfaces **13**, 13392 (2021).

[28] Y. Wang, Z. Zhou, T. Wen, Y. Zhou, N. Li, F. Han, Y. Xiao, P. Chow, J. Sun, M. Pravica, A. L. Cornelius, W. Yang, and Y. Zhao, J. Am. Chem. Soc. **138**, 15751 (2016).

[29] H. X. Zhang, C. P. Niu, J. Zhang, L. J. Zou, Z. Zeng, and X. L. Wang, Phys. Chem. Chem. Phys. **23**, 9679 (2021).

[30] X. L. Ma, Y. M. Wang, Y. Y. Yin, B. B. Yue, J. H. Dai, J. G. Cheng, J. T. Ji, F. Jin, F. Hong, J.-T. Wang, Q. M. Zhang, and X. H. Yu, Sci. China-Phys. Mech. Astron. **64**, 297011 (2021).

[31] M. J. Coak, D. M. Jarvis, H. Hamidov, A. R. Wildes, J. A. M. Paddison, C. Liu, C. R. S. Haines, N. T. Dang, S. E. Kichanov, B. N. Savenko, S. Lee, M. Kratochvílová, S. Klotz, T. C. Hansen, D. P. Kozlenko, J.-G. Park, and S. S. Saxena, Phys. Rev. X **11**, 011024 (2021).

[32] N. C. Harms, H.-S. Kim, A. J. Clune, K. A. Smith, K. R. O'Neal, A. V. Haglund, D. G. Mandrus, Z. Liu, K. Haule, D. Vanderbilt, and J. L. Musfeldt, npj Quantum Mater. **5**, 56 (2020).

[33] M. J. Coak, D. M. Jarvis, H. Hamidov, C. R. S. Haines, P. Alireza, C. Liu, S. Son, I. Hwang, G. I. Lampronti, and D. Daisenberger, J. Phys.: Condens. Matter **32**, 124003 (2020).

[34] H.-S. Kim, K. Haule, and D. Vanderbilt, Phys. Rev. Lett. **123**, 236401 (2019).

[35] Y. G. Wang, J. J. Ying, Z. Y. Zhou, J. L. Sun, T. Wen, Y. N. Zhou, N. N. Li, Q. Zhang, F. Han, Y. M. Xiao, P. Chow, W. G. Yang, V. V. Struzhkin, Y. S. Zhao, and H.-k. Mao, Nat. Comm. **9**, 1914 (2018).

[36] C. R. S. Haines, M. J. Coak, A. R. Wildes, G. I. Lampronti, C. Liu, P. Nahai-Williamson, H. Hamidov, D. Daisenberger, and S. S. Saxena, Phys. Rev. Lett. **121**, 266801 (2018).

[37] S. V. Ovsyannikov, N. V. Morozova, I. V. Korobeinikov, V. Haborets, R. Yevych, Y. Vysochanskii, and V. V. Shchennikov Dalton Trans. **46**, 4245 (2017).

[38] C. Prescher and V. B. Prakapenka, High Pressure Res. **35**, 223 (2015).

[39] B. A. Hunter, International Union of Crystallography Commission on Powder Diffraction Newsletter No. 20 (Summer 1998), http://www.rietica.org

[40] H. K. Mao, J. Xu, and P. M. Bell, J. Geophys. Res. **91**, 4673 (1986).

[41] G. Kresse and J. Hafner, Phys. Rev. B **47**, 558 (1993).

[42] G. Kresse and J. Furthmüller, Phys. Rev. B **54**, 11169 (1996).

[43] J. P. Perdew, K. Burke, and M. Ernzerhof, Phys. Rev. Lett. **77**, 3865 (1996).

[44] G. Kresse and D. Joubert, Phys. Rev. B **59**, 1758 (1999).

[45] P. E. Blöchl, Phys. Rev. B **50**, 17953 (1994).

[46] A. Togo and I. Tanaka, Scr. Mater. **108**, 1 (2015).

[47] R. Becker, W. Brockner, and H. Schäfer, Z. Naturforsch. A **38**, 874 (1983).

[48] N. R. Werthamer, E. Helfand, and P. C. Hohenberg, Phys. Rev. **147**, 295 (1966).

[49] A. M. Clogston, Phys. Rev. Lett. **9**, 266 (1962).

[50] See Supplemental Material at http://link.aps.org/supplemental/ 10.1103/PhysRevMaterials.7.054801 for details on the representative fitting of the high-pressure XRD patterns, the calculated phonon spectra, high-pressure Raman spectra under different experimental configurations, as well as other supporting data.

[51] F. Birch, Phys. Rev. **71**, 809 (1947).

[52] A. F. Goncharov, and V. V. Struzhkin, J. Raman Spectrosc **34**, 532 (2003).

[53] G. Huang, Y. Zhou, Z.-Y. Dong, W.-J. Li, K.-J. Bu, S. Zhou, T. Wang, X.-J. Lü, and X.-J. Chen, J. Phys. Chem. C **126**, 6344 (2022).

[54] J. H. Aguiar Sousa, B. S. Araújo, R. S. Ferreira, A. San-Miguel, R. S. Alencar, and A. G. Souza Filho, ACS Appl. Nano Mater. **5**, 14464 (2022).

[55] Y. B. Gong, Q. Zhou, X. L. Huang, B. Han, X. P. Fu, H. X. Gao, F. F. Li, and T. Cui, ChemNanoMat **3**, 238 (2017).

[56] J. J. Guo, L. Zhang, T. Fujita, T. Goto, and M. W. Chen, Phys. Rev. B **81**, 060102(R) (2010).

[57] E. Smith and G. Dent, in *Resonance Raman Scattering, Modern Raman Spectroscopy* (Wiley, New York, 2019), Chap. 4, pp. 101.